PAPER

Fabrication of nanosheet-assembled hollow copper–nickel phosphide spheres embedded in reduced graphene oxide texture for hybrid supercapacitors†

Maryam Amiri, Akbar Mohammadi Zardkhoshoui* and
Saied Saeed Hosseiny Davarani ![ORCID] *

Owing to their metalloid characteristics with high electrical conductivity, transition metal phosphides (TMPs) have attracted considerable research attention as prospective cathodes for hybrid supercapacitors. Unfortunately, they usually exhibit low rate performance as well as poor longevity, which does not meet the demands of hybrid supercapacitors. The nanocomposite constructed from reduced graphene oxide (rGO) and TMPs with a highly porous nature can effectively overcome the above-mentioned issues, greatly widening their utilization. In this work, we fabricated nanosheet-assembled hollow copper–nickel phosphide spheres (NH-CNPSs) by the controllable phosphatizing of copper–nickel–ethylene glycol (CN–EG) precursors. Then, porous NH-CNPSs were embedded in rGO texture (NH-CNPS–rGO) to form a unique porous nanoarchitecture. The obtained NH-CNPS–rGO has several advantages benefiting as the cathode electrode, such as (i) the hollow structure as well as porous nanosheets are conducive to fast electrolyte diffusion, (ii) the electrical conductivity of NH-CNPS is further enhanced when coupled with the rGO texture, hence promoting electron transfer in the whole structure, (iii) wrapping NH-CNPSs within the rGO texture endows the nanocomposite with much better structural stability, resulting in longer durability of the electrode, And (iv) the porous structures generated in the nanocomposite provide a perfect space for reducing the mass transfer resistance and accessing the electrolyte, thereby boosting the reaction kinetics. The tests demonstrated that the optimal NH-CNPS–rGO electrode revealed a capacity of up to 1075 C g^{-1}, a superior rate capacity, and exceptional longevity of 94.7%. Moreover, a hybrid supercapacitor (NH-CNPS–rGO‖AC) equipped with the NH-CNPS–rGO-cathode electrode and activated carbon (AC)-anode electrode represented a satisfactory energy density of 64 W h kg^{-1} at 801 W kg^{-1} and amazing longevity (91.8% retention after 13 000 cycles), which endorses the promising potential of NH-CNPS–rGO for high-efficiency supercapacitors. This research showcases an appropriate method to engineer hollow TMP–rGO nanocomposites as effective materials for supercapacitors.

1. Introduction

With the fast depletion of coal and petroleum resources, the utilization of sustainable and clean energy (*e.g.*, geothermal energy, solar, wind, and hydropower) has become very important. However, wind and solar energies have many fundamental drawbacks, such as instability and intermittence, restricting

their direct use.[1,2] Hence, it is imperative to develop high-efficiency energy storage devices (ESDs) to realize energy transfer. With their large-scale applications and ever-increasing importance, ESDs such as sodium-ion batteries, supercapacitors, and lithium-ion batteries are receiving particular attention.[3–5] Due to their notable features such as high safety, fast charge–discharge rates, excellent longevity, and high-power output, supercapacitors are gaining extensive attention.[6–12] Nevertheless, one of the marked disadvantages of supercapacitors is their limited energy density (ED). In general, the ED is proportional to the capacity value (*C*) and voltage (*V*) based on the formula $E = 1/2CV^2$.[13,14] The utilization of battery-type materials (as cathode electrodes) can enhance the capacity value, as well as the production of hybrid supercapacitors can broaden the voltage, thus boosting the

Department of Chemistry, Shahid Beheshti University, G. C., Evin, 1983963113 Tehran, Iran. E-mail: ss-hosseiny@sbu.ac.ir, mohammadi.bahadoran@gmail.com; Fax: +98 21 22431661; Tel: +98 21 22431661

ED.[15–17] Hybrid supercapacitors, as emerging devices, are assembled with a capacitive electrode as the anode and a redox-type (battery-type) electrode as the cathode.[18,19] Hybrid supercapacitors provide the opportunity to obtain relatively high EDs with concurrently excellent power densities. Extensive research has shown that the coexistence of the two different mechanisms (electric double-layer capacitor and battery) originating from new materials has led to improved EDs of hybrid supercapacitors.[20]

Extensive research activities have been devoted to synthesizing different high-performance battery-type materials for hybrid supercapacitors such as transition-metal oxides (TMOs),[21] transition metal sulfides (TMSs),[22] and TMPs[23] during the last few years. Among them, TMPs have recently gained increasing research interest and have been extensively used as cathode materials for hybrid supercapacitors. They possess better capacity and rate performance than those of TMOs and TMSs due to their richer valences, better electronic conductivity, and lower electronegativity.[24] Moreover, they are characterized by a friendly environment, low price, and abundant resources.[24] The widely investigated monometallic phosphides include copper phosphorus (Cu_3P),[25] cobalt phosphorus (Co_2P and CoP),[26,27] and nickel-phosphorus (Ni_7P_3, Ni_2P, Ni_5P_4, and $Ni_{12}P_5$),[23] which show favorable prospects for the utilization in supercapacitors. For example, Xu et al. tested $Ni_2P@C$ as an electrode for a hybrid supercapacitor, which reflected a capacity of 979 C g^{-1}.[28] Chen et al. reported a capacitance of 300.9 F g^{-1} for Cu_3P nanotubes.[29] According to the outcomes of the earlier articles on phosphide-based electrode materials, it is discovered that the performance of mixed-metal phosphide-based electrodes is better than those of the monometal phosphide electrodes owing to the enhanced conductivity as well as rich redox reactions.[23,30] Among these mixed-metal phosphides, NiCo-P is the most widely investigated, which is reported to be a helpful material for hybrid supercapacitors.[31,32] From what we know, mixed copper–nickel phosphide has seldom been investigated as cathode electrodes for hybrid supercapacitors so far, though single copper phosphide and nickel phosphide have been reported to be superior electrode materials for hybrid supercapacitors. Based on these facts, it is of considerable importance to conduct a study on mixed copper–nickel phosphide, and its supercapacitive properties are worth expecting.

Nanostructure engineering is a fascinating strategy to enhance the supercapacitive performance of materials by increasing the number of electroactive sites and promoting mass transport.[33–35] Particularly, hierarchical hollow nanostructures can offer enormous benefits for the fabrication of new materials because they integrate the advantages of hierarchically porous structures and low-dimensional building blocks.[36,37] Among low-dimensional building blocks, nanosheets are favorable nanostructures thanks to their high surface area and fast mass transfer, which is useful for providing more electron/ion-accessible sites.[38] Moreover, hollow nanostructures with large surface areas, excellent permeability, high surface/volume ratios, and plentiful surface electroactive

sites have significant potential for supercapacitors.[39,40] Based on the above-mentioned justifications, nanosheet-assembled hollow copper–nickel phosphide spheres could serve as intriguing materials for supercapacitors.

Besides the reasonable design of hollow structures, the combination of TMPs and carbonaceous materials is another intriguing strategy to obtain materials with enhanced performance.[9,41] Graphene, an attractive two-dimensional carbon nanosheet with a hexagonal lattice, has attracted considerable attention in energy storage fields owing to its good electrochemical stability, superior conductivity, huge surface area, and other promising chemical and physical properties.[42] Nevertheless, the restacking and aggregation phenomena that arise from the π–π interaction between graphene sheets result in a significant loss of specific surface area, presenting a low supercapacitive performance.[43] Assembling graphene and other electrode materials to produce a nanocomposite has been until now well-accepted to be a valuable strategy to address the issue since the embedded component between the graphene sheets can separate them.[42] This nanocomposite probably inherits the benefits of the two components but simultaneously eliminates their relevant drawbacks, which is useful for the enhancement of overall performance.[9,42] Based on the above-mentioned discussion, it is appropriate to design TMP/graphene-based nanocomposites to further boost supercapacitive performance.

Herein, we demonstrate the fabrication of nanosheet-assembled hollow copper–nickel phosphide spheres (NH-CNPSs) embedded in the rGO texture for hybrid supercapacitors. The copper–nickel–ethylene glycol (CN–EG) precursors were first prepared via a solvothermal process. Via controllable phosphating treatment, nanosheet-assembled hollow copper–nickel phosphide spheres (NH-CNPSs) were formed. Finally, NH-CNPSs were embedded between rGO layers, endowing them with a porous yet robust nanostructure with superior conductivity and good mechanical integration. The obtained NH-CNPS–rGO sample possessed the following advantages. (i) The unique porous/hollow architecture could offer huge surface areas, increase the electroactive sites, and promote mass transport, and (ii) the synergetic effect between NH-CNPSs and rGO enabled the composite to have enhanced performance. Due to the synergistic effect between NH-CNPS and rGO layers, NH-CNPS–rGO manifests excellent performance. Moreover, a hybrid supercapacitor fabricated with NH-CNPS–rGO as the cathode and AC as the anode delivers good energy density.

2. Experimental section

2.1. Construction of the NH-CNPSs

In a typical synthesis procedure, 3 mmol $Cu(CH_3COO)_2$ and 2 mmol $Ni(CH_3COO)_2$ were dissolved into a mixed solution of ethylene glycol (30 ml) and ethanol (30 ml) in a glass beaker and kept under stirring for 15 min. Subsequently, the homogeneous mixture was poured into an autoclave and then kept

at 180 °C for 10 h. Then, the as-synthesized sample (labeled as CN-EG32-180 precursor) was centrifuged, carefully washed with ethanol, and dried for 15 h. To get the NH-CNPS, 50 mg CN-EG32-180 precursor and 250.0 mg NaH$_2$PO$_2$·H$_2$O were put in two porcelain boats at the downstream and upstream of the furnace, severally. Afterward, the porcelain boat was heated at 350 °C at a ramp rate of 2 °C min^{-1} for 2 h in an N$_2$ atmosphere. The resultant product was denoted as NH-CNPS-350. Besides, the copper phosphide and nickel phosphide nanostructures were synthesized without adding the nickel and copper sources, respectively using a strategy similar to that employed for NH-CNPS. For comparison, a series of control experiments were conducted, including changing solvothermal temperatures (100, 130, and 160 °C) and phosphating temperatures (150, 250, and 450 °C). In addition, solvothermal temperature was unchanged at 180 °C and several millimole ratios of the Cu(CH$_3$COO)$_2$: Ni(CH$_3$COO)$_2$ (1 : 1, 1 : 2, 2 : 1, and 2 : 3) precursors were synthesized *via* a similar route. The as-prepared product and respective parameters are presented in Tables S1–S3 (ESI†).

2.2. Construction of NH-CNPS–rGO

Graphene oxide was produced by modified Hummers' method, as reported previously.[44] To obtain NH-CNPS–rGO, the NH-CNPS-350 powder (100 mg) was dispersed in water (100 ml) containing ammonium hydroxide (10 ml), followed by stirring overnight. After washing, the sample was well dispersed in water (100 ml) and mixed with 50 ml aqueous graphene oxide suspension with several graphene oxide weights. After stirring for 3 h, the sample was carefully collected by centrifugation and treated at 400 °C for 2 h in an N$_2$ atmosphere. The products were labeled as NH-CNPS–rGO-x, x = 1, 2, and 3 meaning that the weight of graphene oxide is 50, 100, and 200 mg, respectively.

2.3. Structural characterization

The morphology and structure of the products were characterized by FE-SEM (MIRA 3 TESCAN, 15 kV, Czech) and TEM (Philips CM200 instrument), respectively. The crystallinity of the as-prepared Cu$_3$P, Ni$_2$P, and NH-CNPS–rGO samples was tested by X-ray diffraction (XRD, Philips X'Pert Pro X-ray diffractometer). Raman pattern of the NH-CNPS–rGO-2 was recorded using a Raman spectrometer (Senterra Bruker) with 785 nm laser excitation. To specify the valence states of the elements in NH-CNPS–rGO-2, an X-ray photoelectron spectrometer (XPS, Thermo Scientific: ESCALAB250Xi Mg X-ray source) was employed. The specific surface area (SA) and pore size distribution of NH-CNPS-350 and NH-CNPS–rGO-2 were identified by the Brunauer–Emmett–Teller (BET) and Barrett–Joyner–Halenda (BJH) methods, respectively (Micromeritics ASAP 2020).

2.4. Electrochemical tests

In the three-electrode configuration, 6 M KOH was utilized as the alkaline electrolyte, a Pt foil as the counter electrode, and Ag/AgCl as the reference electrode. For the working electrode,

based on the optimal mass ratio of 1 : 1 : 8, a conductive filler (acetylene black), adhesive (polyvinylidene fluoride), and materials were fully mixed with the methyl-2-pyrrolidone in a mortar to fabricate the cathode. Subsequently, the as-made paste was evenly coated onto a nickel foam (1 cm × 1 cm), and then the nickel foam coated with slurry was dried at 70 °C for 15 h. Thereafter, it was pressed with a hydraulic press under a pressure of 10 MPa. The active substance loading was about 4.0 mg cm^{-2}. A similar process was employed to fabricate the anode (AC). At room temperature, EIS, CV, and GCD profiles were obtained using an Autolab PGSTAT 204 (Echo Chemie, Netherlands).

The specific capacity values of electrodes were obtained by the GCD plot using the following formula:[45]

$$C_s \, (\mathrm{C \, g^{-1}}) = \frac{2I \times \int V \mathrm{d}t}{m \times V} \tag{1}$$

in formula (1), C_s represents the specific capacity (C g^{-1}), m reveals the mass of the active electrode (g), dt manifests the discharge duration (s), I indicates the discharge current (A), and V signifies the voltage window (V). Besides, the coulombic efficiency (CE) of the NH-CNPS–rGO-2 and hybrid supercapacitor was estimated using formula (2):[33]

$$\mathrm{CE} = \frac{t_d}{t_c} \tag{2}$$

where t_c and t_d represent the time of charge and time of discharge, respectively.

2.5. Designing of NH-CNPS–rGO-2‖AC

The hybrid supercapacitor was assembled by using a nickel foam coated with NH-CNPS–rGO-2, capacitance-type AC, and 6 M KOH aqueous electrolyte as the cathode, anode, and electrolyte, severally. Before the building of NH-CNPS–rGO-2‖AC, the electrodes were soaked in KOH to disclose the maximum electrochemical performance of the device.[46] Noted, the fabricated electrodes were carefully separated with a cellulose paper to avoid a short circuit.[46] Finally, the electrodes and cellulose paper were packed in a non-conductive bag with a hot sealer to fabricate devices. Before the construction of NH-CNPS–rGO-2‖AC, it is very important to balance the charges to obtain high efficiency for the fabricated apparatus. For the as-designed apparatus, the mass ratio of optimized NH-CNPS–rGO-2 to AC was determined from the principle of charge balance ($Q_+ = Q_-$) according to calculation formula (3):[45]

$$\frac{m_+}{m_-} = \frac{C_- \times \Delta V_-}{C_{s_+}} \tag{3}$$

where m (g), ΔV (V), C (F g^{-1}), and C_s (C g^{-1}) represent the mass of electrode materials, voltage window, specific capacitance, and specific capacity, respectively. Note that, + demonstrates the cathode material, while − presents the anode material. From eqn (3), the mass ratio of NH-CNPS–rGO-2 and AC is 1 : 5.7. In NH-CNPS–rGO-2‖AC, the mass loading of NH-CNPS–rGO-2 and AC is 4 and 23.25 mg, severally. The

energy density (E, W h kg^{-1}) and power density (P, W kg^{-1}) of the as-made NH-CNPS–rGO-2‖AC were calculated using formulas (4) and (5):[45]
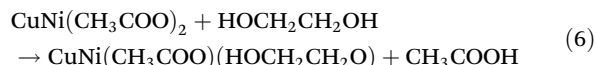
$$E\,(\mathrm{W\,h\,kg^{-1}}) = \frac{I\int V\mathrm{d}t}{3.6\times M} \tag{4}$$

$$P\,(\mathrm{W\,kg^{-1}}) = \frac{E}{\Delta t}\times 3600. \tag{5}$$

3. Results and discussion

Fig. 1a reflects the preparation procedure of the NH-CNPS–rGO-2 sample. With the increase in the reaction temperature, the acetic acid group of metal acetate was gradually replaced with the ethylene glycol group.[47,48] The formation of CuNi-glycolate is as follows:[47]

$$\begin{aligned} &\mathrm{CuNi(CH_3COO)_2 + HOCH_2CH_2OH} \\ &\rightarrow \mathrm{CuNi(CH_3COO)(HOCH_2CH_2O) + CH_3COOH} \end{aligned} \tag{6}$$

$$\begin{aligned} &\mathrm{CuNi(CH_3COO)(HOCH_2CH_2O) + HOCH_2CH_2OH} \\ &\rightarrow \mathrm{CuNi(HOCH_2CH_2O)_2 + CH_3COOH} \end{aligned} \tag{7}$$

$$\begin{aligned} &\mathrm{CuNi(CH_3COO)(HOCH_2CH_2O)} \\ &\rightarrow \mathrm{CuNi(OCH_2CH_2O)_2 + CH_3COOH.} \end{aligned} \tag{8}$$

Based on the above-mentioned analysis, it is concluded that copper–nickel acetate as the copper–nickel source can yield a CuNi-glycolate precursor. Then, NH-CNPSs were *in situ* formed *via* phosphorization heat-treatment using NaH$_2$PO$_2$·H$_2$O,

Fig. 1 (a) Schematic diagram of the fabrication of NH-CNPS–rGO-2. (b and c) FE-SEM images of NH-CNPS–rGO-2. (d–f) TEM images of NH-CNPS–rGO-2. (g–k) EDX mapping of NH-CNPS–rGO-2.

where CuNi-glycolate precursors serve as the self-sacrificial templates. In this process, $NaH_2PO_2 \cdot H_2O$ generates PH_3 (phosphine), which then reacts with a $CuNi(OCH_2CH_2O)_2$ precursor to yield NH-CNPSs. Finally, the NH-CNPSs are embedded between rGO layers to form the NH-CNPS–rGO composite. There is a hypothesis that a positively charged ammonium interlayer is sandwiched between NH-CNPSs and rGO sheets, facilitating electrostatic interactions between the NH-CNPSs and the rGO sheets.[49] The NH-CNPS–rGO composite was prepared via the following mechanism. With ammonium hydroxide present, the alkoxide oxygen functionalities on the surface of rGO sheets interact strongly with the NH^{4+} ions, acting as an electrostatic layer to link the oxy metal-based nanoparticles. This forms a strong interaction network at NH-CNPS–rGO$^-$, stabilizing the proposed architectural design.[49,50] As a result of creating such a nanostructure, the internal stress is cushioned during volume changes, preventing stacking of rGO and thereby making the composite more conductive. Besides, electrochemical tests demonstrated that the as-fabricated composite revealed a positive synergism between rGO and porous NH-CNPS, resulting in excellent pseudocapacitive behaviour in terms of high capacity, excellent rate performance, and good durability.[51] Using this strategy, we can obtain NH-CNPS–rGO-2 characterized by the good conductivity and large surface area, which are beneficial to boost cycle lifespan and rate property for supercapacitors. Morphological observations of the as-synthesized products were conducted by using FE-SEM and TEM at different magnifications. To investigate the process of formation of the precursor and finally regulate the structure of the phosphide products, we tuned the temperature during the fabrication of the precursor. A range of precursors were synthesized at several solvothermal temperatures (100, 130, 160, and 180 °C). When the solvothermal temperature is 100 °C, ultra-small nanosheets appear on the surface of spheres (Fig. S1a in ESI†). With the solvothermal temperature is elevated to 130 °C, the surface of nanosheets in the sample becomes rough (Fig. S1b†). When the solvothermal temperature is increased to 160 °C, the obtained nanosheets become larger (Fig. S1c†). When prolonging the solvothermal temperature to 180 °C, porous nanospheres assembled by well-defined nanosheets are obtained (Fig. S1d†). Fig. S2† depicts the TEM images of precursors at several reaction temperatures. After solvothermal treatment at 100 °C, the hollow structure of the spheres can be observed and the surface of the hollow spheres is composed of nanosheets (Fig. S2a†). As shown in Fig. S2b,† the products are still hollow spheres but reflect a much rougher surface. When the solvothermal temperature is extended to 160 °C, the porosity of the nanostructures becomes higher (Fig. S2c†). After solvothermal treatment of the precursor at 180 °C, the hollow spheres are wrapped with porous nanosheets (Fig. S2d†). The morphological evolutions of the precursors, synthesized with several millimole ratios of $Cu(CH_3COO)_2/Ni(CH_3COO)_2$ at 180 °C, were analyzed by FE-SEM (Fig. S3†). When the millimole ratio of $Cu(CH_3COO)_2/Ni(CH_3COO)_2$ was set to 1 : 1 (denoted as CN-EG11-180), the nanosheets with rough nature were observed on the spheres

(Fig. S3a†). After the millimole ratio of $Cu(CH_3COO)_2/Ni(CH_3COO)_2$ was set to 1 : 2 (denoted as CN-EG12-180), FE-SEM image displayed smaller nanosheets on the spheres with less aggregation (Fig. S3b†). Moreover, when the millimole ratio of $Cu(CH_3COO)_2/Ni(CH_3COO)_2$ was adjusted to 2 : 1 (denoted as CN-EG21-180), the image showed that the precursors still retain the spherical shape and spheres composed of randomly nanosheets (Fig. S3c†). After the mmol ratios of $Cu(CH_3COO)_2/Ni(CH_3COO)_2$ was adjusted to 2 : 3 (denoted as CN EG23-180), the surface of spheres is evenly covered with nanosheets with a rougher surface (Fig. S3d†). The interior structure of CN-EG11-180, CN-EG12-180, CN-EG21-180, and CN-EG23-180 samples were characterized by TEM, which are reflected in Fig. S4.† Fig. S4a† manifests the TEM of CN-EG11-180, in which the hollow spheres are composed of random nanosheets. The TEM image of the CN-EG12-180 display that the as-prepared particles have a hollow sphere morphology with small nanosheet-assembled surface subunits (Fig. S4b†). As shown in the TEM image of CN-EG21-180 in Fig. S4c,† the as-synthesized spheres are composed of nanosheets. Obviously, CN-EG23-180 reflects a hollow morphology with interconnected nanosheets, as manifested in Fig. S4d.† The structure of the as-synthesized products can be tuned via changing phosphorization temperatures. Fig. S5a† reveals the FE-SEM image of the sample obtained by treating CN-EG32-180 at 150 °C. The morphology of the sample does not change compared with CN-EG32-180. With the temperature elevated to 250 °C, the surface of nanosheets in the sample becomes more porous (Fig. S5b†). The FE-SEM images demonstrate that the NH-CNPS well inherit the spherical morphology of their precursors but the nanosheets formed on the spheres become highly porous (Fig. S5b†). From the FE-SEM images, it can be seen that the porosity of the nanosheets becomes increases with the increase in reaction temperature, demonstrating the simultaneous growth of nanosheets on the hollow spheres. As the temperature is elevated to 450 °C, the porous structures partly collapse (Fig. S5c†). Fig. S6† indicates the TEM images of samples obtained by treating CN-EG32-180 at several phosphorization temperatures. After phosphorization treatment at 150 °C, the surface of the hollow spheres is covered with nanosheets (Fig. S6a†). When the temperature is elevated to 250 °C, it can be seen that the sample still maintains the spherical structure of CN-EG32-180 nanospheres, and the surface of these hollow nanospheres is assembled by porous nanosheets (Fig. S6b†). When prolonging the phosphorization temperature to 450 °C, the TEM image displays that the product has a hollow sphere morphology assembled from nanosheets (Fig. S6c†). The morphology of the optimized NH-CNPS-350 was studied by FE-SEM. As shown in the FE-SEM image (Fig. S7a†), the NH-CNPS-350 sample displays a spherical structure. From the magnified image (Fig. S7b†) of one single NH-CNPS-350 particle, it can be seen that the obtained spheres are constructed by highly porous nanosheets. The TEM images (Fig. S6(c and d)†) present that the hollow sphere is made up of porous nanosheets. Moreover, the surface of nanosheets becomes highly porous due to the gases

escaping during the phosphating process (Fig. S7e†). Fig. S8† displays the FE-SEM images of single Ni_2P and Cu_3P samples. For both samples, the surface of nanospheres is fully covered with nanosheets. The TEM images of single Ni_2P and Cu_3P samples reveal that hollow spheres are assembled by porous nanosheets (Fig. S9†). In Fig. S10,† the EDX spectrum of NH-CNPS-350 revealed the elemental signals of Cu, Ni, P, and O with atomic percentages of 43.12%, 27.32%, 27.35%, and 2.21%, severally, which corroborates the successful fabrication of NH-CNPS-350. Besides, according to the atomic percentages of the Cu, Ni, and P elements in NH-CNPS-350, it can be proved that the NH-CNPS-350 sample is composed of Cu_3P and Ni_2P. The EDX analysis of NH-CNPS-350 (Fig. S10†) reflects that the contents of Cu, Ni, P, and O elements in NH-CNPS-350 are about 42.98 wt%, 34.86 wt%, 21.04 wt%, and 1.12 wt%. Therefore, the contents of Cu_3P and Ni_2P in NH-CNPS-350 were calculated as about 53.5 wt% and 45.38 wt%, respectively. Moreover, the surface morphology of NH-CNPS–rGO was characterized using the FE-SEM. As evidenced in Fig. 1b, when the mass ratio of the rGO is 50%, the NH-CNPS nanostructures are encapsulated in the rGO texture and separated from each other to form the well-defined 3D skeleton. It can be observed from the magnified image that the NH-CNPS–rGO inherits the spherical morphology of NH-CNPS, while the NH-CNPS nanostructures are encapsulated in rGO sheets (Fig. 1c). Furthermore, when the mass ratio of rGO is 33% (NH-CNPS–rGO-1), it can be observed that the NH-CNPS nanostructures aggregate with each other (Fig. S11a†). As highlighted in Fig. S11b,† when the mass ratio of the rGO is increased (NH-CNPS–rGO-3), the NH-CNPS nanostructures are still separated, but the obtained nanostructures

are wrapped by a large amount of rGO. As expected, the NH-CNPS nanostructures encapsulated in the rGO layer can also be found in the TEM images in Fig. 1d–f, and the rGO sheets are around the NH-CNPS-350 nanostructures. Owing to the extremely thin as well as flexible nature of the rGO texture, the NH-CNPS-350 nanostructures can still be observed, demonstrating that the intimate contact between NH-CNPS-350 and rGO texture can be obtained. The existing rGO sheets around NH-CNPS nanostructures not only served as the good conductive layer to enhance the conductivity of the composite but also acted as the protective agent to prevent the aggregation of NH-CNPS nanostructures.[9] Moreover, the EDX mapping images disclose that Cu, Ni, P, and C elements are dispersed on NH-CNPS–rGO-2, respectively, as reflected in Fig. 1g–k.

The XRD technique was used to analyze the crystal nature of the pure Cu_3P, pure Ni_2P, and NH-CNPS–rGO-2 samples. The XRD pattern of the NH-CNPS–rGO-2 shown in Fig. 2a demonstrates that the peaks at 36.25° (112), 39.36° (202), 41.75° (211), 45.12° (300), 46.55° (113), 47.35° (212), 52.45° (220), 53.75° (221), 56.65° (311), 59.12° (222), 66.75° (223), 69.55° (321), 73.35° (322), and 78.35° (314) belong to the Cu_3P phase (JCPDS no. 02-1263),[52] and the signals at 40.7° (111), 44.25° (201), 54.52° (300), 55.4° (211), 66.1° (310), 72.17° (311), and 75.01° (400) are attributed to the Ni_2P phase (JCPDS no. 03-0953).[53] Moreover, the XRD pattern of NH-CNPS–rGO-2 reflects the characteristic signal of rGO at 24.8° (002), which can be endorsed by comparison with the pattern of the rGO.[54,55] Moreover, the XRD patterns of pure Cu_3P and Ni_2P samples are displayed in Fig. S12.† These XRD patterns suggest that Cu_3P and Ni_2P were successfully synthesized. The
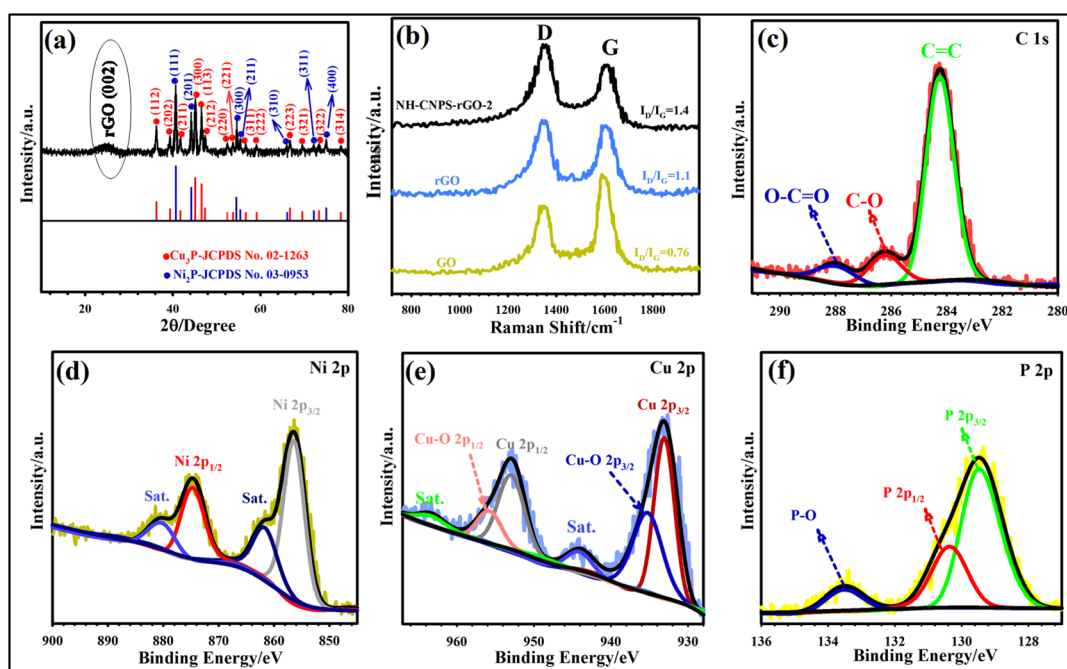

Fig. 2 (a) XRD pattern of NH-CNPS–rGO-2. (b) Raman patterns of NH-CNPS–rGO-2, rGO and GO. (c) C 1s XPS spectra of NH-CNPS–rGO-2. (d) Ni 2p XPS spectra of NH-CNPS–rGO-2. (e) Cu 2p XPS spectra of NH-CNPS–rGO-2. (f) P 2p XPS spectra of NH-CNPS–rGO-2.

XRD results of pure Cu_3P, pure Ni_2P, and NH-CNPS–rGO-2 indicate the existence of Cu_3P and Ni_2P phases in the NH-CNPS–rGO-2 sample. Raman spectra were also recorded to demonstrate the structure composition of samples. Fig. 2b depicts the Raman patterns of NH-CNPS–rGO-2, graphene oxide, and rGO. Two discernible peaks at ~1349 and ~1594 cm^{-1} correspond to the G band and the D band, verifying the sp^2 hybridized carbon atoms and the existence of the disordered graphite carbon, respectively.[54,55] As illustrated in Fig. 2b, the I_D/I_G ratio of rGO (1.1) and NH-CNPS–rGO-2 (1.4) is higher than that of graphene oxide (0.76), corroborating that graphene oxide was converted into rGO.[56] The elemental information of NH-CNPS–rGO-2 can also be determined from XPS results. Fig. S13† displays the survey profile of NH-CNPS–rGO-2 with the signals of Ni 2p, Cu 2p, P 2p, C 1s, and O 1s, which reflects the existence of Ni, Cu, P, C, and O in NH-CNPS–rGO-2. The deconvoluted C 1s pattern reveals three signals, which relate to C–C/C=C (284.34 eV), C–O (286.22 eV), and O–C=O (287.98 eV) bonds, respectively (Fig. 2c).[54] The deconvolution of Ni reflected two recognizable peaks at 856.52 eV (Ni 2p$_{3/2}$) and 874.72 eV (Ni 2p$_{1/2}$), confirming the existence of divalent nickel (Ni^{2+}) in Ni_2P. The peaks at 861.9 and 879.78 eV can also be attributed to the satellite peaks (Fig. 2d).[57] The Cu 2p spectrum (Fig. 2e) manifests two discernible peaks at 952.81 and 932.95 eV, which are indexed to Cu 2p$_{1/2}$ and Cu 2p$_{3/2}$ of Cu_3P, severally. The other peaks at 935.18 and 955.3 eV are related to oxidized copper due to surface oxidation in air. The peaks at 944.21 and 963.27 eV are also considered as the satellite peaks.[58] Fig. 2f depicts the P 2p spectrum, in which the peaks at 130.45 and 129.65 eV can be related to the metal–P (M = Cu or Ni) bond in P 2p$_{1/2}$ and P 2p$_{3/2}$.[59] Another P 2p signal located at 133.62 eV was related to the oxidized phosphorus species due to the surface oxidation of NH-CNPS–rGO-2 when contacted with the air. It should be noted that the binding energy of Ni^{2+} in the as-fabricated NH-CNPS–rGO-2 is slightly higher in the energy state than bare nickel phosphide, which refers to charge transfer from nickel to copper *via* a d–d (metal-to-metal charge-transfer) transition, which can impact the charge storage capacity of the NH-CNPS–rGO-2 sample.[59] The XPS analysis reveals a strong electronic interaction between Cu_3P and Ni_2P in the sample, demonstrating a synergistic effect that helps to improve the electrochemical performance.[60,61] To validate the porous structure of optimized NH-CNPS-350 and NH-CNPS–rGO-2, the pore size distribution and N_2 absorption–desorption isotherms were characterized, as indicated in Fig. S14.† As evidenced in Fig. S14,† the obtained graphs can be attributed to type IV with a noticeable hysteresis loop, signifying a mesoporous structure.[6,9,10] NH-CNPS–rGO-2 reflected a higher surface area (SA) of 302.1 m^2 g^{-1} compared to NH-CNPS-350 (203.2 m^2 g^{-1}), which could be attributed to the presence of rGO. The pore-size distribution of NH-CNPS-350 and NH-CNPS–rGO-2 samples was obtained by BJH, as manifested in Fig. S14 (inset).† The NH-CNPS–rGO-2 possesses a pore size of 7.11 nm, corroborating its mesoporous nature.[6,9,10] Moreover, the NH-CNPS-350 presents a pore size of 8.02 nm. The large SA and porous

texture of NH-CNPS–rGO-2 can offer more electron channels, shorter ion-transfer paths, and rich active sites, beneficial to the good electrochemical performance.[62,63]

The supercapacitive performances of the as-made electrodes are studied in the configuration of the 3-electrode test cell. Fig. S15a† manifests the CV plots of CN-EG32-100, CN-EG32-130, CN-EG32-160, and CN-EG32-180-based electrodes at 60 mV s^{-1}. The enclosed CV area of CN-EG32-180 is larger than that of other samples, confirming the higher capacity of the CN-EG32-180. Besides, judging from the GCD patterns, CN-EG32-180 showed a longer discharge time (Fig. S15b†) compared with CN-EG32-100, CN-EG32-130, and CN-EG32-160, validating the higher capacity of CN-EG32-180. Moreover, the capacity of CN-EG32-180 was obtained from GCD plots reaching 278 C g^{-1}, which is better than those of CN-EG32-100 (197 C g^{-1}), CN-EG32-130 (220.5 C g^{-1}), CN-EG32-160 (254 C g^{-1}) (Fig. S15c†). Based on the above-mentioned results, the CN-EG32-180-based electrode is considered as the optimized precursor. The comparative CV graphs of CN-EG32-180, CN-EG21-180, CN-EG11-180, CN-EG23-180, and CN-EG12-180 at 60 mV s^{-1} are reflected in Fig. S16a.† As manifested in Fig. S16a,† CN-EG32-180 depicts a larger integrated area compared with other precursors, reflecting its greater capacity. Besides, it can be observed from the GCD profiles that CN-EG32-180 possesses a longer discharge time than that of other precursors (Fig. S16b†). At 1 A g^{-1}, CN-EG32-180 manifested a capacity of 278 C g^{-1}, whereas the CN-EG21-180, CN-EG11-180, CN-EG23-180, and CN-EG12-180 electrodes demonstrated 266, 240, 218, and 195 C g^{-1}, severally (Fig. S16c†). Accordingly, the CN-EG32-180 precursor is considered as the optimized precursor. Fig. S17a† highlights the comparison of the CV plots of phosphide samples at 60 mV s^{-1}. The area integrated from CVs is in the following order: NH-CNPS-350 > NH-CNPS-250 > NH-CNPS-150 > NH-CNPS-450. An identical result can be obtained from the GCD profiles at 1 A g^{-1} (Fig. S17b†), in which NH-CNPS-350 possesses a longer discharge time than that of other products. At 1 A g^{-1}, the NH-CNPS-350 revealed a capacity of 800 C g^{-1}, whereas NH-CNPS-250, NH-CNPS-150, and NH-CNPS-450 electrodes exhibited 770, 735.5, and 697.5 C g^{-1}, severally (Fig. S17c†). According to the above-mentioned tests, NH-CNPS-350 is considered as the optimized sample. The CV and GCD of NH-CNPS–rGO-1, NH-CNPS–rGO-2, and NH-CNPS–rGO-3 tested at 60 mV s^{-1} and 1 A g^{-1}, severally, are compared in Fig. S18a and b.† NH-CNPS–rGO-2 demonstrated a larger CV area as well as a longer discharge time than those the NH-CNPS–rGO-1, and NH-CNPS–rGO-3 electrodes, indicating its better performance compared to the products. At 1 A g^{-1}, capacity values of 1075, 1045, and 1010 C g^{-1} for the NH-CNPS–rGO-2, NH-CNPS–rGO-1, and NH-CNPS–rGO-3 electrodes, severally were obtained (Fig. S18c†). Fig. 3a displays the CV profiles of the pure nickel foam, NH-CNPS-350, and NH-CNPS–rGO-2 electrodes at 60 mV s^{-1} measured in the voltage window of (0 to 0.60) V *vs.* Ag/AgCl. As highlighted in Fig. 3a, the nickel foam has no visible capacity performance, which reveals that the good capacity performances of the elec-
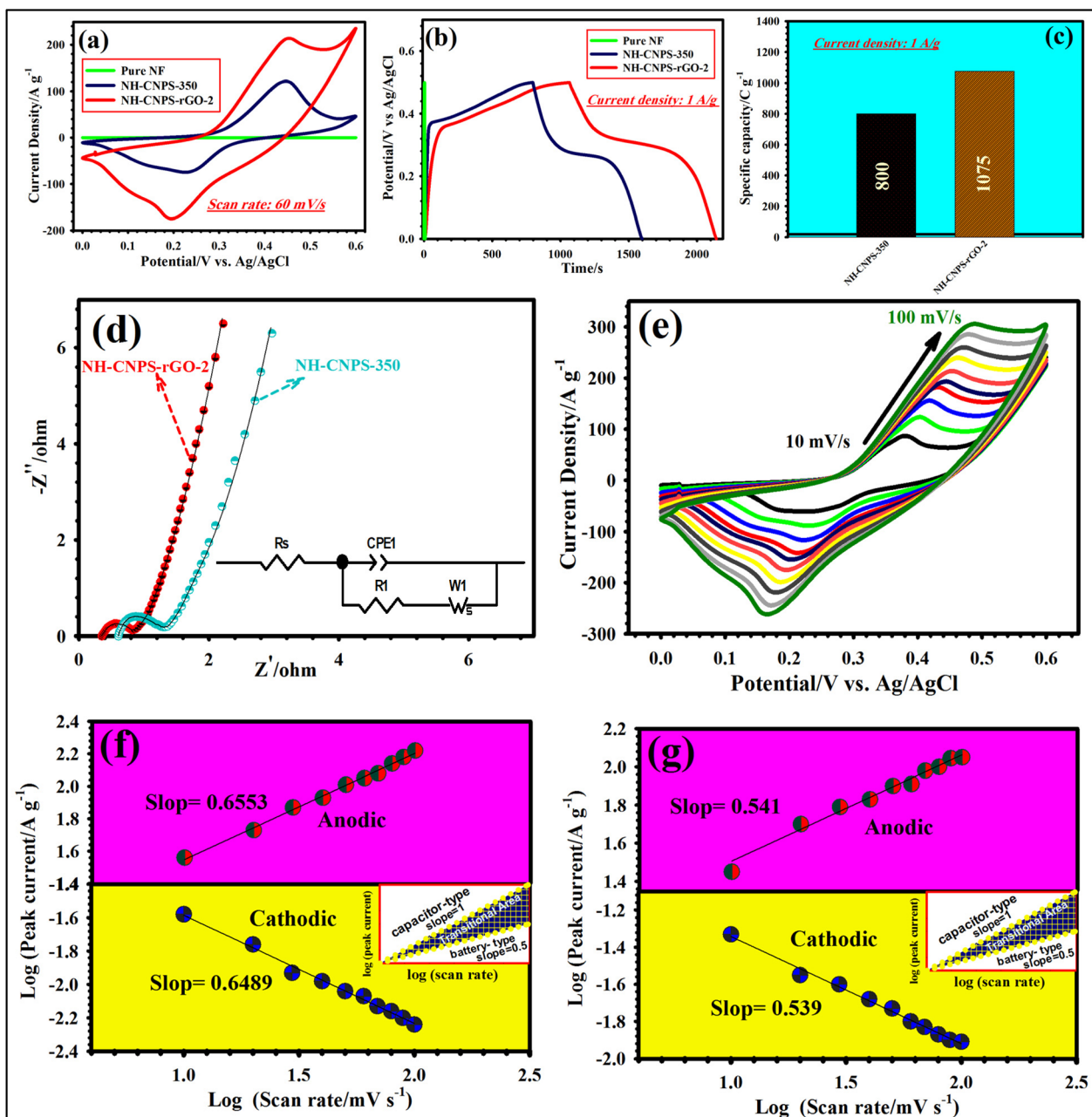
Fig. 3 (a) CV plots of the pure nickel foam, NH-CNPS-350, and NH-CNPS–rGO-2 electrodes at 60 mV s^{-1}. (b) GCD plots of the pure nickel foam, NH-CNPS-350 and NH-CNPS–rGO-2 electrodes at 1 A g^{-1}. (c) Specific capacities of NH-CNPS-350 and NH-CNPS–rGO-2 electrodes at 1 A g^{-1}. (d) Nyquist plots of the NH-CNPS-350 and NH-CNPS–rGO-2 electrodes (inset reveals the equivalent circuit model). (e) CV plots of the NH-CNPS–rGO-2 electrode from 10 to 100 mV s^{-1}. (f) Linear relation between the plot of the logarithm(i) *versus* logarithm(v) of the NH-CNPS–rGO-2 electrode. (g) Linear relation between the plot of the logarithm(i) *versus* logarithm(v) of the NH-CNPS-350 electrode.

trodes originated from the active materials.[6–10] The CV curve of the NH-CNPS-350 electrode possesses discernible reduction and oxidation peaks, corresponding to the faradaic redox reactions of the material (Cu^{+}/Cu^{2+}, Ni^{2+}/Ni^{3+}). Moreover, the redox peaks disclose the battery-like nature of the NH-CNPS-350 electrode. These faradaic redox peaks originated from the following reaction:[57]

$$NiCuP + OH^{-} \leftrightarrow NiP\text{–}OH + CuP\text{–}OH + e^{-}. \qquad (9)$$
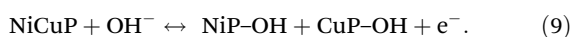
Moreover, the peak current and integrated CV area of the NH-CNPS–rGO-2 are greater than those of the other as-made electrodes, implying its good energy storage capacity. Such good performance of NH-CNPS–rGO-2 results from its unique properties such as high SSA, highly porous texture, and excellent conductivity.[64] The compared GCD plots (Fig. 3b) demonstrate that the NH-CNPS–rGO-2 electrode possesses the longest discharge time, affirming its higher capacity. The capacity values of NH-CNPS-350 and NH-CNPS–rGO-2 were compared

at 1 A g^{-1}, as manifested in Fig. 3c. The NH-CNPS–rGO-2 revealed a capacity as high as 1075 C g^{-1} when compared with 800 C g^{-1} of the NH-CNPS-350 electrode. Such excellent capacity value of NH-CNPS–rGO-2 originated from its special features including high SSA, good catalytic activity, unique porous networks, and the good synergy between NH-CNPS and rGO skeleton.[64] The EIS measurements (Fig. 3d) were conducted to understand the charge transfer behavior as well as electrical conductivity in various electrodes. The EIS data were fitted by utilizing the Z-view software. Moreover, the relevant equivalent circuit is illustrated in Fig. 3d (inset). As evidenced in Fig. 3d, the curves consisted of the quasi-semicircle (in a high-frequency phase) and the nearly direct line (in a low frequency phase). The intersection of the graphs with the X-axis referred to the internal resistance (R_s), manifesting the resistance between the electrode materials and electrolyte,[9] at the time the diameter of the quasi-semicircle presented the charge transfer resistance (R_{ct}).[10,11] According to Fig. 3d, it can be observed that NH-CNPS–rGO-2 had a lower R_s (0.35 Ω) than that of NH-CNPS-350 (0.61 Ω), signifying a higher conductivity. Moreover, a smaller R_{ct} (0.44 Ω) for the NH-CNPS–rGO-2 than that of NH-CNPS-350 (0.70 Ω) implies a faster charge transfer kinetics.[9,10] The slope of the line (low-frequency phase) corresponds to the Warburg resistance (R_W), which was associated with diffusion resistance of the ions near the surface of the electrode during redox processes.[65] Remarkably, the NH-CNPS–rGO-2 electrode disclosed steeper plots than that of the NH-CNPS-350 electrode, implying a lower R_W.[65] By analyzing the CV graphs of NH-CNPS–rGO-2 (Fig. 3e), it can be found that the oxidation/reduction peak shift to a higher/lower potential state along with the sweep speeds increasing owing to the polarization and ohmic resistance.[66] Simultaneously, the CV graphs still keep the well symmetrical and similar profile with the enhancement of the scanning speed, implying excellent reversibility and good rate capability.[65,66] Furthermore, the CV graphs of the as-fabricated electrodes from 10 to 100 mV s^{-1} are represented in Fig. S19.† To discern the charge storage mechanism of the NH-CNPS-350 and NH-CNPS–rGO-2 electrodes, the kinetic behavior of both electrodes is affirmed by fitting the CV graphs under miscellaneous sweep speeds as stated by the following power-law equation:[67,68]

$$\log i_p = \log a + b \log(v) \qquad (10)$$

where b and a are the adjustable parameters, v is the sweep speed and i_p is the peak current.[67,68] The value of b can be used to discern the charge storage mechanism and varies between 0.5 and 1.0. When $b = 0.5$, the reaction is influenced by the ion diffusion process; when $b = 1$, the reaction reflects the surface-controlled capacitive behavior.[67,68] The slope of the linear graph of log(i) vs. log(v) specifies the value of b. As illustrated in Fig. 3f, the b values of NH-CNPS–rGO-2 based on the corresponding cathodic and anodic peaks are 0.6489 and 0.6553, respectively. Moreover, b values for the cathodic and anodic peaks of the NH-CNPS-350 electrode are 0.539 and

0.541, respectively (Fig. 3g). The estimated b values of NH-CNPS–rGO-2 are larger than 0.50, which reveals that redox reactions of NH-CNPS–rGO-2 demonstrated the diffusion-controlled as well as surface-controlled kinetics. In addition, the results indicated that the b-values of NH-CNPS-350 are lower than that of NH-CNPS–rGO-2, confirming that the pseudocapacitance-type behavior of NH-CNPS-350 reinforced after the introduction of rGO layer.

Fig. 4a highlights the GCD graphs of NH-CNPS–rGO-2 measured at miscellaneous applied current densities (1, 2.5, 5, 7.5, 15, and 30 A g^{-1}). As reflected in Fig. 4a, a distinct charge–discharge platform and a symmetric nature can be found in the GCD graphs, further emphasizing the battery-type behavior and excellent electrochemical reversibility of the NH-CNPS–rGO-2 electrode.[9,10] Furthermore, the GCD graphs of the other electrode materials are manifested in Fig. S20.† Fig. 4b manifests the capacities of the NH-CNPS–rGO-2 in comparison with NH-CNPS-350 at 1, 2.5, 5, 7.5, 15, and 30 A g^{-1}, measured from the GCD graphs. The NH-CNPS–rGO-2 disclosed the capacity values of 1075, 1062.5, 1035, 980, 915.25, and 852.5 C g^{-1} at 1, 2.5, 5, 7.5, 15, and 30 A g^{-1}, severally, which were better than that of NH-CNPS–rGO-1 and NH-CNPS–rGO-3 (Fig. S21a†), and superior to reported TMP-based electrodes (Fig. 4c) and Table S4 in ESI.†[7,32,69–74] In detail, NH-CNPS-350 reflected the capacities of 800, 775, 735.5, 660, 605.25, and 574 C g^{-1} at 1, 2.5, 5, 7.5, 15, and 30 A g^{-1}, severally, which were higher than those of NH-CNPS-150, NH-CNPS-250 and NH-CNPS-450 electrodes (Fig. S21b†). Even at 30 A g^{-1}, the NH-CNPS–rGO-2 electrode maintained 79.3% of its initial capacity value, which is better than that of NH-CNPS–rGO-1 (76.55%) and NH-CNPS–rGO-3 (73.9%) (Fig. S21a†). The results indicate that NH-CNPS-350 has a rate performance of 71.75%, which is higher than that of NH-CNPS-250 (70.23%), NH-CNPS-150 (69.9%), and NH-CNPS-450 (68.1%) (Fig. S21b†). Cycling longevity was a basic parameter for the electrodes in supercapacitors. Therefore, the as-designed electrodes were checked for their longevity until 13 000 GCD cycles (at 15 A g^{-1}). As evidenced in Fig. 4d, the NH-CNPS–rGO-2 electrode shows a 94.7% capacity retention after 13 000 cycles, and the Coulomb efficiency attains 99.4%, displaying its excellent longevity and good electrochemical reversibility. Moreover, NH-CNPS–rGO-1 and NH-CNPS–rGO-3 retain 92.5%, and 90.9% capacity retention, respectively (Fig. S22a†). NH-CNPS-350 retains 83.5% of its initial capacity value after 13 000 cycles (Fig. S22b†), whilst NH-CNPS-250, NH-CNPS-150, and NH-CNPS-450 retain 81.6%, 78.8%, and 76.4%, severally (Fig. S22b†). The inset in Fig. 4d manifests the first and last 5 GCD graphs, revealing a perfect GCD graph with battery-like nature, and also signifying impressive coulombic efficiency. For further confirmation of the good longevity of NH-CNPS–rGO-2, the EIS plots of the NH-CNPS–rGO-2 were obtained after the 1st and 13 000th cycle (Fig. 4e). Based on the EIS results, the R_{ct} values for NH-CNPS–rGO-2 were noticed to be 0.44 and 0.601 Ω before and after the 13 000 cycles, respectively. Besides, the R_s values for this sample were observed to be 0.35 and 0.40 Ω before and after

Fig. 4 (a) GCD plots of the NH-CNPS–rGO-2 electrode from 1 to 30 A g^{-1}. (b) Specific capacities *vs.* current densities of the NH-CNPS–rGO-2 and NH-CNPS-350 electrodes. (c) Comparison of capacity values of NH-CNPS–rGO-2 with the results previously reported in the literature. (d) Longevity and coulombic efficiency of NH-CNPS–rGO-2 at 15 A g^{-1} (the inset illustrates the first and last 5 GCD cycles). (e) Nyquist curves of NH-CNPS–rGO-2 before and after 13 000 GCD cycles.

the 13 000 cycles, severally. To study any degradation of the NH-CNPS–rGO-2 after 13 000 cycles, we obtained the FE-SEM of this material after 13 000 cycles, and the images are manifested in Fig. S23a.† As represented in Fig. S23a,† the morphology of the NH-CNPS–rGO-2 still maintains its structure, and the NH-CNPS nanostructures are encapsulated in the rGO skeleton after 13 000 cycles, which reveals the prevention of NH-CNPS nanostructures from degradation due to the existence of the rGO skeleton. Moreover, the FE-SEM images of the NH-CNPS-350 were collected after 13 000 cycles as displayed in

Fig. S23b.† The above-mentioned results affirmed that the supercapacitive performance of the NH-CNPS–rGO-2 sample can be effectively enhanced by controlling the morphology of the materials. Specifically, the exceptional performance of the NH-CNPS–rGO-2 electrode can be ascribed to several features: (1) the hollow structure along with porous nanosheets considerably increased the SSA and provided richer active sites, enhancing the rate capability,[65] (2) the highly porous texture of the NH-CNPS–rGO-2 sample shortened the ion transportation pathway, and accelerated the faradaic redox reaction,[66] (3) the

surface nanosheets and internal cavity can withstand structural distortion and accommodate mechanical strain based on the continual GCD test, ensuring the cycling longevity of the electrode material,[65] (4) synergistic effect of the bimetallic is beneficial for the enhancement of conductivity and active sites, thereby achieving high capacity and rate capability,[69] (5) the wrapping of the rGO skeleton bridges each NH-CNPS nanostructure together to produce a three-dimensional (3D) conductive structure, accelerating the electron transport and hence promoting the fast reactions,[9,10] and (6) the rGO sheets can effectively act as the space separator to impede the aggregation of NH-CNPS nanostructures, which is helpful to the infiltration of the KOH electrolyte within the electrode, thereby enhancing the ion diffusion rate within the electrode.[9] The electrochemical tests of the AC anode electrode were measured by using a 3-electrode cell in KOH. The CV graphs of the AC were obtained in a potential window of −1 to 0 V from 10 to 100 mV s^{-1}, as manifested in Fig. S24a.† As highlighted in Fig. S24a,† the collected graphs reflect an almost rectangular nature, demonstrating a typical electrical double-layer capacitance behavior. The GCD profiles (Fig. S24b†) present a symmetric triangular shape, indicating good reversibility. Fig. S24c† illustrates the specific capacitances of the AC elec-

trode from 1 to 30 A g^{-1}. At 1 A g^{-1}, the AC electrode reflects the capacitance of 185 F g^{-1}, and at 30 A g^{-1}, the electrode displays the capacitance of 139.5 F g^{-1}.

To prove the functionality of NH-CNPS–rGO-2 as the electrode in effective devices, a cathode electrode of NH-CNPS–rGO-2, an anode electrode of AC electrode, and a cellulose paper separator were combined to produce a hybrid supercapacitor (NH-CNPS–rGO-2‖AC). Fig. 5a manifests a schematic diagram of NH-CNPS–rGO-2‖AC. It is extremely important to determine an appropriate working voltage of NH-CNPS–rGO-2‖AC. Fig. 5b highlights the individual CV graphs of NH-CNPS–rGO-2 and AC electrodes, which are tested at 60 mV s^{-1}. The findings infer that the voltage window of the NH-CNPS–rGO-2 electrode is between 0 and 0.6 V, while the AC electrode is between 0.0 and −1.0 V. Therefore, a feasible voltage window of 1.6 V can be adopted. To further corroborate the obtained cell voltage of NH-CNPS–rGO-2‖AC, the CV graphs under various voltage cells were collected at 5 mV s^{-1}, which is reflected in Fig. 5c. As depicted in Fig. 5c, the voltage window of 1.6 V is a proper cell voltage for NH-CNPS–rGO-2‖AC because oxidation reaction can be viewed at higher voltages. The shape of CV graphs just reflects insignificant changes with sweep speed variating in the settled cell voltage

Fig. 5 (a) Schematic diagram of NH-CNPS–rGO-2‖AC. (b) CV graphs of AC (anode electrode) and NH-CNPS–rGO-2 (cathode electrode) at 60 mV s^{-1} in a 3-electrode cell. (c) CV graphs of the NH-CNPS–rGO-2‖AC at various cell voltages at 5 mV s^{-1} from 1.2 to 2.0 V. (d) CV graphs of NH-CNPS–rGO-2‖AC at various sweep rates from 5 to 80 mV s^{-1}. (e) GCD plots of NH-CNPS–rGO-2‖AC at different current densities from 1 to 30 A g^{-1}. (f) Variation of capacities of NH-CNPS–rGO-2‖AC as a function of current densities. (g) Longevity and coulombic efficiency of NH-CNPS–rGO-2‖AC at 15 A g^{-1} (the inset reflects the first and last 5 GCD cycles). (h) Comparison of the NH-CNPS–rGO-2‖AC device's Ragone plot with various devices.
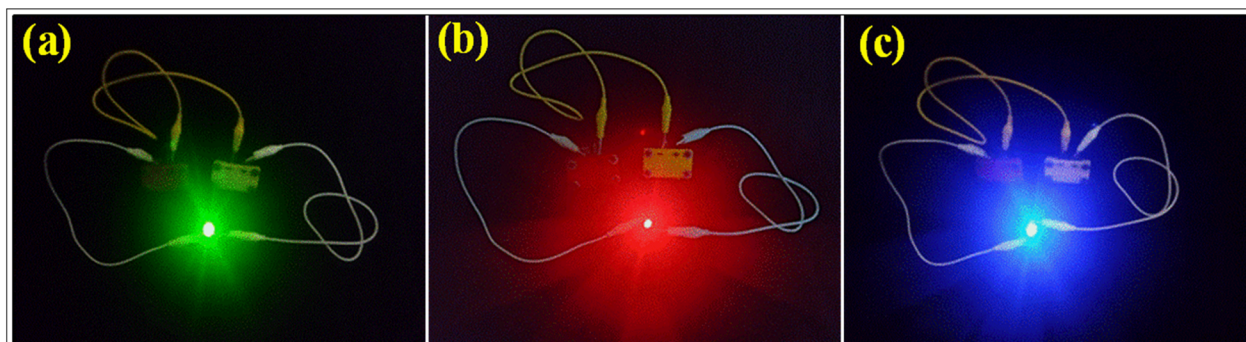
Fig. 6 (a) Photograph of the green LED with two NH-CNPS–rGO-2‖AC devices connected in series. (b) Photograph of the red LED with two NH-CNPS–rGO-2‖AC devices connected in series. (c) Photograph of the blue LED with two NH-CNPS–rGO-2‖AC devices connected in series.

(0–1.6 V, Fig. 5d), demonstrating the high reversibility and good rate performance of NH-CNPS–rGO-2‖AC.[63,64] It is important to note that all the graphs combine the CV graph characteristics of EDLC as well as battery-like materials. As depicted in Fig. 5e, the GCD profiles of the NH-CNPS–rGO-2‖AC retain good symmetry at a cell voltage as high as 1.6 V, suggesting good electrochemical reversibility and coulombic efficiency. The specific capacities of NH-CNPS–rGO-2‖AC were estimated to be 288, 281.6, 268.8, 256, 240, and 221.2 C g^{-1} at 1, 2.5, 5, 7.5, 15, and 30 A g^{-1}, respectively, confirming 76.8% retention of the capacity (Fig. 5f). The longevity of the as-designed NH-CNPS–rGO-2‖AC explored at 15 A g^{-1} is reflected in Fig. 5g. Surprisingly, the capacity retention is 91.8% together with 98.1% coulombic efficiency after 13 000 cycles. Besides, Fig. 5g (inset) depicts the first and last 5 cycles of the GCD graphs, corroborating the high reversibility and coulombic efficiency of NH-CNPS–rGO-2‖AC. Fig. 5h is the Ragone plot, which manifests the association between the energy density and power density of NH-CNPS–rGO-2‖AC. The assembled NH-CNPS–rGO-2‖AC displays the remarkable energy density of 64 W h kg^{-1} at a good power density of 801 W kg^{-1} and remains 49.15 W h kg^{-1} even at a pretty high power density (24 575 W kg^{-1}). The excellent energy density of NH-CNPS–rGO-2‖AC can be compared with the reported TMP-based supercapacitors (Fig. 5h and Table S4, ESI†).[30,75–81] Fig. S25a and b† depict the CV and GCD graphs of the single and two NH-CNPS–rGO-2‖AC devices connected in series and parallel at a scan rate of 80 mV s^{-1} and a current density of 1 A g^{-1}, respectively. Compared with the single NH-CNPS–rGO-2‖AC device (1.6 V), the output of two NH-CNPS–rGO-2‖AC devices connected in series displayed a larger potential window of 3.2 V. In the case of the parallel connections, the output current (CV graphs) and discharge time (GCD graphs) of the two NH-CNPS–rGO-2‖AC devices connected in parallel are enlarged by a factor of two compared with the NH-CNPS–rGO-2‖AC single device. The obtained results demonstrated that the as-fabricated NH-CNPS–rGO-2‖AC devices could be connected in parallel or in series to drive different electronic devices.

To endorse the practicability of NH-CNPS–rGO-2‖AC, the green (2.9 V), red (1.8 V), and blue (3 V) light-emitting diodes (LEDs) can be lightened (Fig. 6, see Video S1 in ESI†) by con-

necting two charged NH-CNPS–rGO-2‖AC devices in series. Fig. 6 indicates the illumination of the green (up to 3 min), red (up to 4 min) and blue (up to 3 min) LEDs after charging (30 s) the two-series-connected NH-CNPS–rGO-2‖AC devices.

4. Conclusions

In this work, nanosheet-assembled hollow copper–nickel phosphide spheres (NH-CNPSs) were embedded between rGO skeletons (NH-CNPS–rGO) to form a unique composite. The NH-CNPS–rGO not only illustrated a high specific surface area to offer more active sites, but also exhibited a highly porous nature to shorten the ion transfer pathway, effectively boosting the supercapacitive performance. Besides, the wrapping of the rGO skeleton on the surface of NH-CNPSs not only improves the conductivity but also inhibits the aggregation of NH-CNPSs and preserves the structural stability. This work proved the functional superiority of the NH-CNPS–rGO in comparison with the NH-CNPS sample in terms of capacity, rate performance, electrical conductivity, and longevity. This is evidence that the existence of rGO in the synthetic process could considerably improve the overall supercapacitive performance. Based on the splendid performance of the NH-CNPS–rGO electrode, a hybrid supercapacitor with a good energy density of 64 W h kg^{-1} at 801 W kg^{-1} was successfully assembled using NH-CNPS–rGO-2 and AC as the cathode and anode electrodes, respectively. From our perspective, the proposed approach and findings can open the way for the development of high-efficiency hybrid supercapacitors using various porous materials.

Conflicts of interest

The authors declare no competing financial interest.

Acknowledgements

References

1 S. Kumar and A. Misra, *Nanoscale*, 2021, **13**, 19453–19465.

2 G. P. Ojha, B. Pant, J. Acharya and M. Park, *Nanoscale*, 2021, **13**, 19537–19548.

3 M. Amiri, S. E. Moosavifard, S. S. Hosseiny Davarani and M. Shamsipur, *Energy Fuels*, 2021, **35**, 15108–15117.

4 H. Qi, C. Zhao, J. Huang, C. He, L. Tang and W. Deng, *Nanoscale*, 2022, **14**, 780–789.

5 Q. Du, Y. Zhao, K. Zhuo, Y. Chen, L. Yang, C. Wang and J. Wang, *Nanoscale*, 2021, **13**, 13285–13293.

6 A. Mohammadi Zardkhoshoui, B. Ameri and S. S. Hosseiny Davarani, *Nanoscale*, 2021, **13**, 2931–2945.

7 M. Amiri, S. E. Moosavifard, S. S. Hosseiny Davarani, S. Kamari Kaverlavani and M. Shamsipur, *Chem. Eng. J.*, 2021, **420**, 129910.

8 M. Amiri, S. S. Hosseiny Davarani, S. Kamari Kaverlavani, S. E. Moosavifard and M. Shamsipur, *Appl. Surf. Sci.*, 2020, **527**, 146855.

9 A. Mohammadi Zardkhoshoui and S. S. Hosseiny Davarani, *Nanoscale*, 2020, **12**, 12476–12489.

10 A. Mohammadi Zardkhoshoui and S. S. Hosseiny Davarani, *Sustainable Energy Fuels*, 2021, **5**, 900–913.

11 M. Amiri, S. S. Hosseiny Davarani, S. E. Moosavifard and Y.-Q. Fud, *J. Colloid Interface Sci.*, 2022, **616**, 141–151.

12 A. Mohammadi Zardkhoshoui, S. S. Hosseiny Davarani, M. Maleka Ashtiani and M. Sarparast, *J. Mater. Chem. A*, 2019, **7**, 10282–10292.

13 A. Mohammadi Zardkhoshoui, M. Maleka Ashtiani, M. Sarparast and S. S. Hosseiny Davarani, *J. Power Sources*, 2020, **450**, 227691.

14 M. Amiri, A. Mohammadi Zardkhoshoui, S. S. Hosseiny Davarani, M. Maghsoudi and M. K. Altafi, *Sustainable Energy Fuels*, 2022, **6**, 3626–3642.

15 A. Mohammadi Zardkhoshoui, B. Ameri and S. S. Hosseiny Davarani, *Chem. Eng. J.*, 2022, **435**, 135170.

16 A. Mohammadi Zardkhoshoui, B. Ameri and S. S. Hosseiny Davarani, *Chem. Eng. J.*, 2021, **422**, 129953.

17 B. Ameri, A. Mohammadi Zardkhoshoui and S. S. Hosseiny Davarani, *Mater. Chem. Front.*, 2021, **5**, 4725–4738.

18 D. P. Chatterjee and A. K. Nandi, *J. Mater. Chem. A*, 2021, **9**, 15880–15918.

19 L. Wang, R. Zhang, Y. Jiang, H. Tian, Y. Tan, K. Zhu, Z. Yu and W. Li, *Nanoscale*, 2019, **11**, 13894–13902.

20 N. Jayababu, S. Jo, Y. Kim and D. Kim, *ACS Appl. Mater. Interfaces*, 2021, **13**, 19938–19949.

21 M. Kandasamy, S. Sahoo, S. K. Nayak, B. Chakraborty and C. S. Rout, *J. Mater. Chem. A*, 2021, **9**, 17643–17700.

22 P. Kulkarni, S. K. Nataraj, R. G. Balakrishna, D. H. Nagarajua and M. V. Reddy, *J. Mater. Chem. A*, 2017, **5**, 22040–22094.

23 A. Agarwal and B. R. Sankapal, *J. Mater. Chem. A*, 2021, **9**, 20241–20276.

24 S. K. T. Aziz, S. Kumar, S. Riyajuddin, K. Ghosh, G. D. Nessim and D. P. Dubal, *J. Phys. Chem. Lett.*, 2021, **12**, 5138–5149.

25 A. Mohammadi Zardkhoshoui and S. S. Hosseiny Davarani, *Dalton Trans.*, 2020, **49**, 10028–10041.

26 M. Cheng, H. Fan, Y. Xu, R. Wang and X. Zhang, *Nanoscale*, 2017, **9**, 14162–14171.

27 T. Shu, H. Gao, Q. Li, F. Wei, Y. Ren, Z. Sun, J. Qi and Y. Sui, *Nanoscale*, 2020, **12**, 20710–20718.

28 F. Xu, Q. Xia, G. Du, Z. Fan and N. Chen, *Electrochim. Acta*, 2021, **380**, 138200.

29 Y.-C. Chen, Z.-B. Chen, Y.-G. Lin and Y.-K. Hsu, *ACS Sustainable Chem. Eng.*, 2017, **5**, 3863–3870.

30 S. Li, M. Hua, Y. Yang, W. Huang, X. Lin, L. Ci, J. Lou and P. Si, *J. Mater. Chem. A*, 2019, **7**, 17386–17399.

31 J. Liu, X. Deng, S. Zhu, N. Zhao, J. Sha, L. Ma and F. He, *Electrochim. Acta*, 2021, **368**, 137528.

32 P. Li, M. Zhang, H. Yin, J. Yao, X. Liu and S. Chen, *Appl. Surf. Sci.*, 2021, **536**, 147751.

33 B. Ameri, A. Mohammadi Zardkhoshoui and S. S. Hosseiny Davarani, *Dalton Trans.*, 2021, **50**, 8372–8384.

34 A. Mohammadi Zardkhoshoui and S. S. Hosseiny Davarani, *Nanoscale*, 2020, **12**, 1643–1656.

35 A. Mohammadi Zardkhoshoui, S. S. Hosseiny Davarani, M. Maleka Ashtiani and M. Sarparast, *ACS Sustainable Chem. Eng.*, 2019, **78**, 7908–7917.

36 B. Y. Guan, L. Yu and X. W. Lou, *Angew. Chem., Int. Ed.*, 2017, **56**, 2386.

37 B. Y. Guan, X. Y. Yu, H. B. Wu and X. W. Lou, *Adv. Mater.*, 2017, **29**, 1703614.

38 S. Zhao, Y. Wang, J. Dong, C.-T. He, H. Yin, P. An, K. Zhao, X. Zhang, C. Gao, L. Zhang, J. Lv, J. Wang, J. Zhang, A. M. Khattak, N. A. Khan, Z. Wei, J. Zhang, S. Liu, H. Zhao and Z. Tang, *Nat. Energy*, 2016, **1**, 16184.

39 L. Yu, X. Y. Yu and X. W. Lou, *Adv. Mater.*, 2018, **30**, 1800939.

40 P. Zhang, S. Wang, B. Guan and X. W. Lou, *Energy Environ. Sci.*, 2019, **12**, 164.

41 A. Mohammadi Zardkhoshoui, S. S. Hosseiny Davarani and A. A. Asgharinezhad, *Dalton Trans.*, 2019, **48**, 4274–4282.

42 K. Wang, K. N. Hui, K. S. Hui, S. Peng and Y. Xu, *Chem. Sci.*, 2021, **12**, 5737–5766.

43 Y. Xu, C. Chen, Z. Zhao, Z. Lin, C. Lee, X. Xu, C. Wang, Y. Huang, M. I. Shakir and X. Duan, *Nano Lett.*, 2015, **15**, 4605–4610.

44 D. C. Marcano, D. V. Kosynkin, J. M. Berlin, A. Sinitskii, Z. Sun, A. Slesarev, L. B. Alemany, W. Lu and J. M. Tour, *ACS Nano*, 2010, **4**, 4806–4814.

45 L. Wan, Y. Wang, Y. Zhang, C. Du, J. Chen, Z. Tian and M. Xie, *Chem. Eng. J.*, 2021, **415**, 128995.

46 S. C. Sekhar, B. Ramulu, S. J. Arbaz, S. K. Hussain and J. S. Yu, *Small Methods*, 2021, **5**, 2100335.

47 M. Zhu, X. Li, C. Tu, Q. Luo, Y. Nie, J. Pan and S. Li, *Mater. Chem. Front.*, 2022, **6**, 203–212.

48 Z. Y. Liu, A. P. Wu, H. J. Yan, D. N. Su, C. X. Jin, H. Guo, L. Wang and C. G. Tian, *Chem. Commun.*, 2020, **56**, 2913–2916.

49 G. Pagot, K. Vezzù, A. Nale, M. Fauri, A. Migliori, V. Morandi, E. Negro and V. D. Noto, *J. Electrochem. Soc.*, 2020, **167**, 070547.

50 N. Katir, A. Benayad, D. Rouchon, N. Marcotte, N. E. Brahmi, J. P. Majoral, M. Bousmina and A. E. Kadib, *Nanoscale Adv.*, 2019, **1**, 314–321.

51 S. Al-Rubaye, R. Rajagopalan, S. X. Dou and Z. Cheng, *J. Mater. Chem. A*, 2017, **5**, 18989–18997.

52 S. Wei, K. Qi, Z. Jin, J. Cao, W. Zheng, H. Chen and X. Cui, *ACS Omega*, 2016, **1**, 1367–1373.

53 Y. Lu, X. Wang, Y. Mai, J. Xiang, H. Zhang, L. Li, C. Gu, J. Tu and S. X. Mao, *J. Phys. Chem. C*, 2012, **116**, 22217–22225.

54 Z. Tahmasebi, A. Mohammadi Zardkhoshoui and S. S. Hosseiny Davarani, *Dalton Trans.*, 2021, **50**, 12168–12178.

55 Z. Tahmasebi, A. Mohammadi Zardkhoshoui and S. S. Hosseiny Davarani, *Catal. Sci. Technol.*, 2021, **11**, 1814–1826.

56 M. Zhu, Q. Yan, X. Bai, H. Cai, J. Zhao, Y. Yan, K. Zhu, K. Ye, J. Yan, D. Cao and G. Wang, *J. Colloid Interface Sci.*, 2022, **608**, 922–930.

57 H. M. El Sharkawy, D. M. Sayed, A. S. Dhmees, R. M. Aboushahba and N. K. Allam, *ACS Appl. Energy Mater.*, 2020, **3**, 9305–9314.

58 J. Li, X. Li, P. Liu, X. Zhu, R. N. Ali, H. Naz, Y. Yu and B. Xiang, *ACS Appl. Mater. Interfaces*, 2019, **11**, 11442–11450.

59 L. Yan, H. Jiang, Y. Xing, Y. Wang, D. Liu, X. Gu, P. Dai, L. Li and X. Zhao, *J. Mater. Chem. A*, 2018, **6**, 1682–1691.

60 S. Riyajuddin, K. Azmi, M. Pahuja, S. Kumar, T. Maruyama, C. Bera and K. Ghosh, *ACS Nano*, 2021, **15**, 5586–5599.

61 M. Afshan, S. Kumar, D. Rani, M. Pahuja, R. Ghosh, S. A. Siddiqui, S. Riyajuddin and K. Ghosh, *ACS Appl. Nano Mater.*, 2022, **5**, 15328–15340.

62 K. Li, B. Zhao, H. Zhang, H. Lv, J. Bai, H. Ma, P. Wang, W. Li, J. Si, X. Zhu and Y. Sun, *Adv. Funct. Mater.*, 2021, **31**, 2103073.

63 Y. Wen, Y. Liu, T. Wang, Z. Wang, Y. Zhang, X. Wu, X. Chen, S. Peng and D. He, *ACS Appl. Energy Mater.*, 2021, **4**, 6531–6541.

64 Y. A. Haj, J. Balamurugan, N. H. Kim and J. H. Lee, *J. Mater. Chem. A*, 2019, **7**, 3941–3952.

65 P. Li, S. Liu, Y. Mao, H. Yin, S.-M. Chen and X. Liu, *ACS Appl. Energy Mater.*, 2021, **4**, 9178–9189.

66 L. Lyu, W. H. Antink, B.-H. Lee, C. W. Kim, E. Jung, K.-D. Seong, T. Hyeon and Y. Piao, *ACS Appl. Energy Mater.*, 2021, **4**, 10553–10564.

67 J. Y. Dai, S. B. Singh, N. H. Kim and J. H. Lee, *J. Mater. Chem. A*, 2021, **9**, 27503–27517.

68 J. Acharya, G. P. Ojha, B. Pant and M. Park, *J. Mater. Chem. A*, 2021, **9**, 23977–23993.

69 M. Xie, M. Zhou, Y. Zhang, C. Du, J. Chen and L. Wan, *J. Colloid Interface Sci.*, 2022, **608**, 79–89.

70 Y. Zhao, H. Dong, J. Yu, R. Chen, Q. Liu, J. Liu, R. Li, X. Wang and J. Wang, *Electrochim. Acta*, 2021, **390**, 138840.

71 Q. Zhou, Y. Gong and K. Tao, *Electrochim. Acta*, 2019, **320**, 134582.

72 L. Wan, Y. Wang, Y. Zhang, C. Du, J. Chen, M. Xie, Z. Tian and W. Zhang, *J. Power Sources*, 2021, **506**, 230096.

73 X. Shi, L. Sun, X. Zhang, J. Qian, J. Hu, F. Xie, H. Zhang and Y. Zhang, *J. Energy Storage*, 2022, **54**, 105302.

74 M. Li, Y. Luo, C. Jia, Q. Zhang, G. Luo, L. Zhao, R. Boukherroub and Z. Jiang, *J. Alloys Compd.*, 2022, **893**, 162340.

75 H. C. Chen, S. Jiang, B. Xu, C. Huang, Y. Hu, Y. Qin, M. He and H. Cao, *J. Mater. Chem. A*, 2019, **7**, 6241–6249.

76 Y. Dong, X. Yue, Y. Liu, Q. Zheng, Z. Cao and D. Lin, *J. Colloid Interface Sci.*, 2022, **628**, 222–232.

77 S. He, Z. Li, H. Mi, C. Ji, F. Guo, X. Zhang, Z. Li, Q. Du and J. Qiu, *J. Power Sources*, 2020, **467**, 228324.

78 F. Wang, H. Lei, H. Peng, J. Zhou, R. Zhao, J. Liang, G. Ma and Z. Lei, *Electrochim. Acta*, 2019, **325**, 134934.

79 X. Zhang, L. Zhang, G. Xu, A. Zhao, S. Zhang and T. Zhao, *J. Colloid Interface Sci.*, 2020, **561**, 23–31.

80 S. Gayathri, P. Arunkumar, D. Saha and J. H. Han, *J. Colloid Interface Sci.*, 2021, **588**, 557–570.

81 J. Xu, N. Yang, S. Yu, A. Schulte, H. Schönherr and X. Jiang, *Nanoscale*, 2020, **12**, 13618–13625.